Journal of Energy Storage 163 (2026) 121774

Contents lists available at ScienceDirect

Journal of Energy Storage

journal homepage: www.elsevier.com/locate/est

Research papers

Architectural control of pyrene-4,5,9,10-tetraone-based conjugated microporous polymers toward high-performance supercapacitors

Yousra M. Nabil [a,b], Shimaa Abdelnaser [a,b], Shiao-Wei Kuo [a], Ahmed F.M. EL-Mahdy [a,b,*]

[a] *Department of Materials and Optoelectronic Science, National Sun Yat-Sen University, Kaohsiung, 80424, Taiwan*
[b] *Chemistry Department, Faculty of Science, Assiut University, Assiut, 71516, Egypt*

ARTICLE INFO

Keywords:
Conjugated microporous polymers
Phenyl linker
Pyrene-4,5,9,10-tetraone
Redox-active polymers
Supercapacitors

ABSTRACT

Architectural control of conjugated microporous polymers (CMPs) offers a powerful strategy for tuning charge transport, ion diffusion, and redox activity in next-generation supercapacitor electrodes. Here, we report two pyrene-4,5,9,10-tetraone/benzo[1,2-b:4,5-b′]dithiophene-4,8-dione (PT/BDTD) CMPs engineered through linker selection: a phenyl-bridged network (PTPh-BDTD) prepared by Suzuki coupling and an ethynylbenzene-linked analogue (PTDE-BDTD) obtained via Sonogashira polymerization. Both CMPs form permanently microporous, π-conjugated frameworks that enable pseudocapacitive charge storage dominated by reversible quinone-type redox chemistry, as supported by electrochemical kinetics and ex situ vibrational analysis. Despite comparable BET surface areas, PTPh-BDTD exhibits tighter packing and more favorable charge-transport characteristics, delivering a high specific capacitance of 410.55 F g^{-1} at 0.5 A g^{-1} and retaining 74.31% of its capacitance after 6000 cycles. Electrochemical impedance analysis reveals faster interfacial kinetics for PTPh-BDTD (Rct = 6.55 Ω), consistent with its higher intrinsic conductivity (9.0 S cm^{-1}). A symmetric supercapacitor assembled from PTPh-BDTD achieves 112.41 F g^{-1} with an energy density of 35.97 Wh kg^{-1} at a power density of 981.06 W kg^{-1} and maintains 91.02% capacitance retention over 4000 cycles. These results highlight linker-driven architectural control as an effective strategy to maximize redox-site utilization and charge transport in CMP electrodes for high-performance supercapacitors.

1. Introduction

The expanding use of renewable energy and portable electronics is driving demand for reliable electrochemical energy-storage systems, particularly to buffer intermittent solar and wind power and provide fast, durable energy delivery [1,2]. Among available systems, supercapacitors (SCs) have attracted considerable attention for modern applications ranging from consumer electronics to electric vehicles and smart grids [3,4]. SCs offer distinct advantages, including high power density, fast charge–discharge capability, and excellent cycling stability [5]. However, improving their energy density while maintaining high-rate performance remains a major challenge, primarily because it is governed by electrode material design. Electrochemical supercapacitors are generally classified into electric double-layer capacitors (EDLCs), pseudocapacitors (PCs), and hybrid or asymmetric capacitors [6,7]. In EDLCs, charge storage occurs through ion adsorption at the electrode surface, typically employing carbon-based materials such as activated carbon, graphene, and carbon nanotubes due to their high surface area and stability. Despite their outstanding power performance, these materials often exhibit limited specific capacitance because of the absence of intrinsic redox-active sites [7,8]. In contrast, pseudocapacitors store energy via fast, reversible Faradaic redox reactions at the electrode–electrolyte interface [9,10]. Metal oxides, MXenes, and conjugated polymers are common pseudocapacitive materials [11–15], but many experience structural degradation, volume changes during ion insertion and extraction, limited rate performance, and poor conductivity [16]. To overcome these limitations, hybrid architectures combining EDLC and pseudocapacitive mechanisms have been developed to enhance energy density and widen operational voltage windows [17–19]. Nevertheless, further improvements require electrode materials that integrate intrinsic electrical conductivity, stable redox-active functionalities, tunable porosity, and robust structural integrity, alongside a clear understanding of structure–performance relationships [20,21].

Conjugated microporous polymers (CMPs) are a class of porous, π-conjugated organic polymers that have attracted growing interest for their precise control of pore size, chemical properties, and overall

---

[*] Corresponding author at: Department of Materials and Optoelectronic Science, National Sun Yat-Sen University, Kaohsiung, 80424, Taiwan.
E-mail address: ahmedelmahdy@mail.nsysu.edu.tw (A.F.M. EL-Mahdy).

https://doi.org/10.1016/j.est.2026.121774
Received 6 December 2025; Received in revised form 15 February 2026; Accepted 22 March 2026

network architecture [22–24]. CMPs typically exhibit pore diameters of ≤2 nm, highly cross-linked network structures, high surface area, redox properties, inherent electrical conductivity, and a fully covalently bonded π-conjugated backbone. The extended π-conjugated framework enables efficient electron delocalization, thereby facilitating rapid charge transport throughout the material. Simultaneously, a well-distributed microporous network provides continuous, accessible pathways for ion diffusion, allowing electrolyte ions to swiftly reach and exit the electrochemically active sites across multiple charging–discharging cycles. This synergistic combination of electronic conductivity and efficient ion transport significantly improves the electrode's rate capability [22]. Although CMPs have been extensively investigated for various applications, including drug delivery, sensors, photocatalysis, dye removal, gas storage, and fluorescence [25–30], their use as supercapacitor electrode materials remains constrained by their intrinsically low electrical conductivity, which substantially diminishes capacitance. The incorporation of redox-active frameworks, including aza-fused rings, porphyrins, phenazines, anthraquinones, and ferrocenes, into CMP structures has been shown to enhance electrical conductivity, improve capacitance performance, and increase chemical durability during charge–discharge cycles [31]. Several coupling techniques can be used to synthesize CMPs, including the Suzuki, Sonogashira, Yamamoto, and Buchwald–Hartwig reactions, as well as oxidative chemical polymerizations [32–34]. These methods allow for accurate management of their building structure and operational attributes. Therefore, the development of high-performance electrodes for advanced supercapacitors with high energy and power densities, exceptional stability, and efficiency relies on a thorough understanding of the correlations between the CMP structural design and their electrochemical characteristics.

This study investigates how architectural control in pyrene-4,5,9,10-tetraone (PT)–based conjugated microporous polymers (CMPs)—specifically linker engineering and structural modulation—governs electrochemical charge storage and transport. Two redox-active CMPs, PTPh-BDTD and PTDE-BDTD, were designed by combining the electron-deficient benzo[1,2-b:4,5-b′]dithiophene-4,8-dione (BDTD) core with the extended π-conjugated PT unit. Structural diversity was introduced by employing a phenyl linker (PTPh-BDTD) versus an ethynylbenzene linker (PTDE-BDTD), enabling a direct comparison of how linker geometry and conjugation pathway influence π–π interactions, charge delocalization, ion accessibility, and pseudocapacitive contributions. As illustrated in Fig. 1, PTPh-BDTD was synthesized via a Suzuki coupling reaction using 2,6-dibromobenzo[1,2-b:4,5-b′]dithiophene-4,8-dione (BDTD-2Br), 1,3,6,8-tetrabromopyrene-4,5,9,10-tetraone (PT-4Br), and benzene-1,4-diboronic acid (Ph-2B$(OH)_2$) while PTDE-BDTD was obtained through Sonogashira–Hagihara polymerization employing BDTD-2Br, PT-4Br, and p-diethynylbenzene (DEPh-2C≡C). The resulting materials were characterized to confirm their chemical structure and porosity, and their electrochemical behavior was evaluated in both three-electrode and device configurations to establish structure–property relationships and clarify the role of linker-controlled architecture in CMP-based supercapacitor electrodes.

2. Results and discussion

2.1. Synthesis and characteristics of materials

The synthetic routes and structural diversity of the monomers 2,6-dibromobenzo[1,2-b:4,5-b′]dithiophene-4,8-dione (BDTD-2Br) and 1,3,6,8-tetrabromopyrene-4,5,9,10-tetraone (PT-4Br) are illustrated in Schemes S1 and S2 and Figs. S1–S6. Two distinct linker types were employed in the polymerization process to construct the target CMPs. The phenyl-linked PTPh-BDTD CMP was synthesized via a Suzuki coupling reaction between BDTD-2Br, PT-4Br, and benzene-1,4-diboronic acid (Ph-2B$(OH)_2$), as shown in Fig. 1 and Scheme S3. In contrast, the ethynyl-linked PTDE-BDTD CMP was prepared through a Sonogashira–Hagihara coupling reaction using BDTD-2Br, PT-4Br, and *p*-diethynylbenzene (DEPh-2C≡C), as presented in Fig. 1 and Scheme S4. Both polymers exhibit cross-linked three-dimensional architectures characterized by intrinsic porosity and strong π–π stacking interactions. The structural composition and chemical bonding of the synthesized BDTD-based CMPs were systematically investigated using Fourier-transform infrared spectroscopy (FT-IR), solid-state ^{13}C cross-polarization/magic-angle spinning nuclear magnetic resonance (^{13}C CP/MAS NMR), and X-ray photoelectron spectroscopy (XPS).

Figs. S7 and S8 display the FT-IR spectra of PTPh BDTD and PTDE

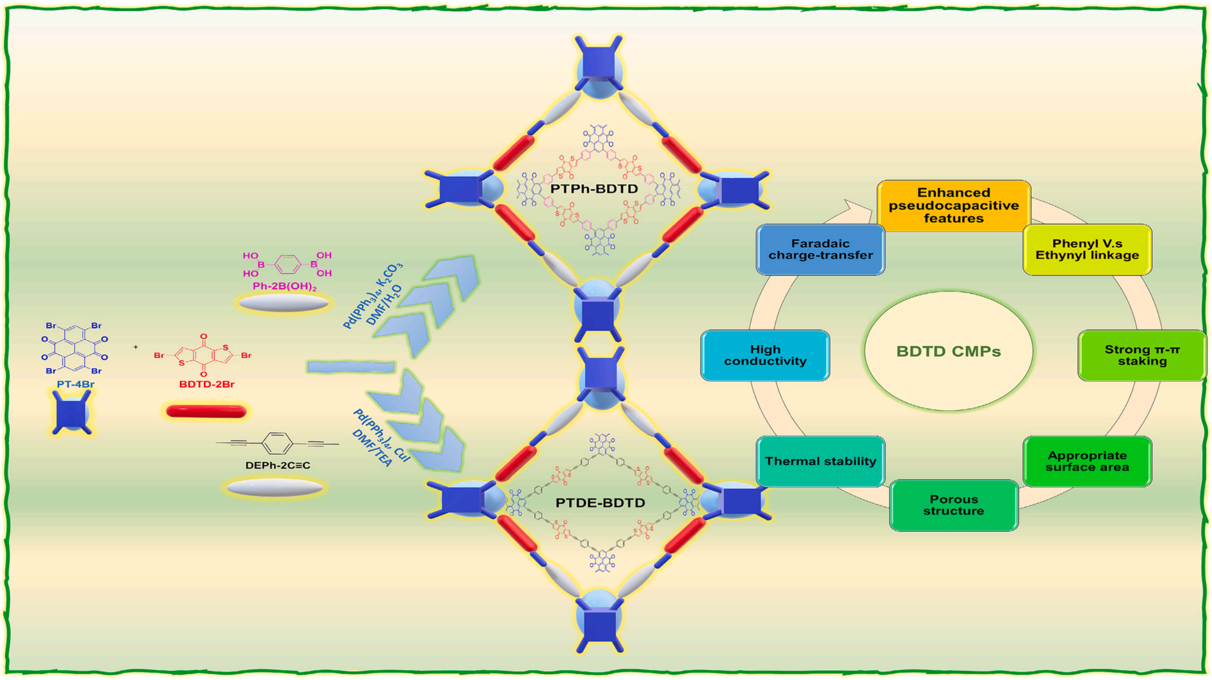

Fig. 1. Schematic approach and molecular framework of PTPh-BDTD and PTDE-BDTD CMPs.

BDTD. In both spectra, the C—Br bands at 577 and 674 cm^{-1} that appear in the BDTD-2Br and PT-4Br monomers are absent, confirming complete consumption of the brominated precursors and successful formation of the CMP networks. In addition, PTPh-BDTD shows no B—O vibration band at 1353 cm^{-1}, indicating the completion of the Suzuki polymerization (Fig. S7). For PTDE-BDTD, the disappearance of the C≡C—H stretching band at 3269 cm^{-1} (a diagnostic signal of the DEPh-2C≡C monomer) further verifies polymer formation. Meanwhile, the presence of the C≡C stretching vibration at 2189 cm^{-1} indicates the successful incorporation of the ethynylbenzene linkage via the Sonogashira coupling reaction (Fig. S8). Moreover, the strong bands at 1652 and 1657 cm^{-1} are assigned to the carbonyl (C═O) stretching vibrations in PTPh-BDTD and PTDE-BDTD, respectively. Both spectra also exhibit aromatic C—H stretching vibrations at 3047–3156 cm^{-1} and aromatic C═C vibrations in the 1390–1520 cm^{-1} region, consistent with the conjugated aromatic frameworks. The solid-state ^{13}C NMR spectra of PTPh-BDTD and PTDE-BDTD CMPs are shown in Fig. 2a. Three main resonance regions are observed at 183–172 ppm, assigned to carbonyl (C═O) carbons, at 154–140 ppm, assigned to aromatic C—X carbons where X is C or S, and at 136–123 ppm, assigned to aromatic C—H carbons. Additionally, we conducted XPS analysis to assess the chemical composition of S, C, and O in PTPh-BDTD and PTDE-BDTD CMPs. Fig. 2b shows four characteristic XPS peaks for PTPh-BDTD at 164.85, 227.82, 283.40, and 529.11 eV and for PTDE-BDTD at 162.11, 228.36, 283.40, and 530.94 eV, corresponding to the S 2p, S 2s, C 1s, and O 1s orbitals, respectively. No additional peaks were detected, indicating the absence of detectable impurities in the BDTD-based CMPs. To further clarify the chemical environments, the C 1s and S 2p spectra were deconvoluted, enabling identification of the different carbon and sulfur species present in the CMP frameworks (Fig. 2c–f, Tables S1 and S2). The high-resolution C 1s spectra were curve-fitted to resolve the carbon environments in the two CMPs. For PTPh-BDTD, four contributions were identified at 283.30, 284.02, 284.58, and 286.80 eV, which can be assigned to C═C, C—S, C—C, and C═O functionalities, respectively. For PTDE-BDTD, five C 1s components were required, appearing at 283.10, 284.11, 284.09, 285.89, and 287.76 eV, consistent with C═C, C—S, C—C, C≡C, and C═O linkages (Fig. 2c and 2d). In the sulfur region, both materials exhibit the characteristic S 2p doublet arising from spin–orbit splitting into S 2p$_{3/2}$ and S 2p$_{1/2}$ with the expected 2:1 area ratio. The PTPh-BDTD spectrum shows peaks at 162.91 eV (S 2p$_{3/2}$) and 164.07 eV (S 2p$_{1/2}$), while PTDE-BDTD displays the corresponding signals at 162.66 and 163.86 eV (Fig. 2e and 2f; Tables S1 and S2). It is worth noting that the proportions of C═O and C—S functionalities in the PTPh-BDTD CMP, 21.66% and 14.43%, respectively, are higher than those in PTDE-BDTD, which exhibits C═O and C—S contents of 16.85% and 11.72% (Table S2). This results in enhanced heteroatom content in the PTPh-BDTD framework, leading to improved capacitive performance [35,36]. Moreover, the theoretical elemental ratios were determined according to the atomic percentages of each element. After applying sensitivity factor corrections, experimental elemental ratios were obtained from the integrated peak areas of each species (C, O, and S) in the XPS survey, with hydrogen excluded because it is undetectable in XPS. Tables S3 and S4 demonstrate strong alignment between theoretical and experimental elemental ratios, validating the effective integration of heteroatoms into the polymer framework. Based on the XPS survey, PTPh-BDTD exhibits a higher heteroatom content, with O and S contents of 17.84% and 12.64%, respectively. In contrast, PTDE-BDTD showed comparatively lower O/S ratios of 14.03% and 8.32%. The XPS results were confirmed by elemental analysis (Table S5), which demonstrated enhanced heteroatom doping in PTPh-BDTD compared to PTDE-BDTD. Higher heteroatom content in PTPh-BDTD increases the number and accessibility of redox-active sites, which helps explain its improved electrochemical performance. In addition, within PTPh-BDTD architecture, thiophene units act as electron-rich donors [37,38], whereas the carbonyl groups within the quinone moieties function as electron acceptors [39]. This donor–acceptor motif accelerates electron and ion transport during charging and discharging, which supports faster kinetics, greater capacity, and more stable long-term cycling [40].

The polymers were characterized using multiple techniques. Nitrogen adsorption–desorption measurements were used to evaluate porosity and calculate the specific surface area, thermogravimetric analysis (TGA) was applied to assess thermal stability, and X-ray diffraction (XRD) was used to examine crystallinity. Nitrogen adsorption–desorption isotherms were further recorded to determine the surface area and pore size distribution of PTPh-BDTD and PTDE-BDTD (Fig. 3a). The nitrogen adsorption–desorption isotherms of PTPh-

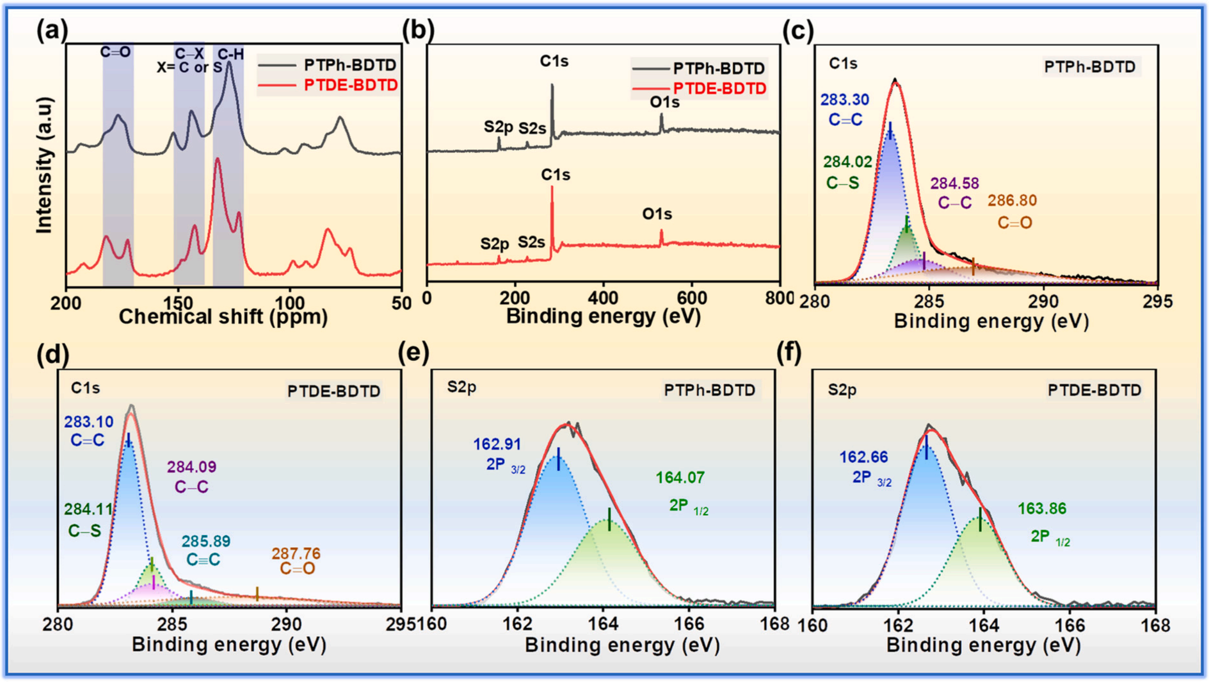

Fig. 2. (a) ^{13}C CP-MAS NMR spectrum, (b–f) XPS patterns (c, d) C 1s, and (e, f) S 2p curves of PTPh-BDTD, PTDE-BDTD CMPs.

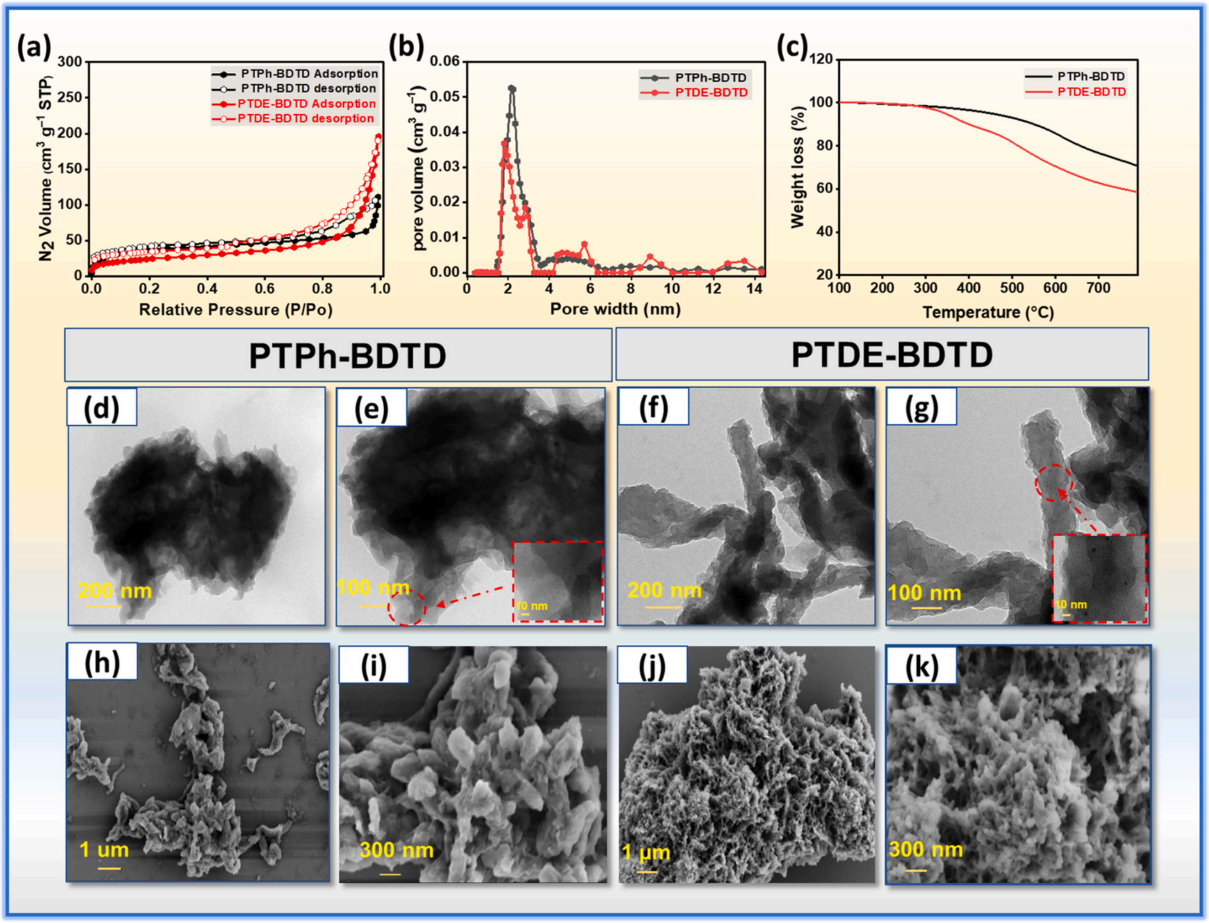

Fig. 3. (a) N_2 adsorption/desorption Isotherms, (b) pore size distribution, (c) TGA curves, (d–g) TEM, and (h–k) SEM images for PTPh-BDTD and PTDE-BDTD CMPs, respectively.

BDTD and PTDE-BDTD show type II behavior, with pronounced uptake at low relative pressure ($P/P_0 < 0.1$) and a sharp increase at high relative pressure ($P/P_0 > 0.84$), suggesting primarily microporous frameworks. PTPh-BDTD exhibits a slightly higher BET surface area of 93.96 $m^2\ g^{-1}$ than PTDE-BDTD (84.46 $m^2\ g^{-1}$) (Fig. 3a). The pore size distribution of PTPh-BDTD shows a dominant pore centered at approximately 2.19 nm with a pore volume of 0.12 $cm^3\ g^{-1}$, whereas PTDE-BDTD displays pores centered at around 1.8 nm with a pore volume of 0.30 $cm^3\ g^{-1}$ (Fig. 3b and Table S6). Overall, these results confirm that the BDTD-based CMPs possess accessible microporosity and appreciable surface area, providing abundant interfacial areas for electrolyte contact and charge storage. Moreover, TGA was used to evaluate the thermal stability of the BDTD-based CMPs under N_2 from 40 to 800 °C. Fig. 3c and Table S7 assess the thermal stability of PTPh-BDTD and PTDE-BDTD CMPs with 5% weight loss at 452.33 °C and 344.62 °C, respectively. Furthermore, their decomposition temperatures at 10% weight were recorded at 550.13 °C and 399.62 °C, respectively. Interestingly, the residual masses for PTPh-BDTD and PTDE-BDTD CMPs were determined to be 70.64% and 58.48%, respectively, after heating to 800 °C, indicating their higher thermal stability. PTPh-BDTD CMP exhibited improved thermal stability as a result of the phenyl bridge introduction in its structure, resulting in a boost in its thermal stability [41]. Moreover, we examined the powder XRD patterns of PTPh-BDTD and PTDE-BDTD CMPs to characterize their crystalline nature. Fig. S9a and b show broad diffraction features, confirming that the CMPs are predominantly amorphous. The interlayer spacing associated with π–π stacking was then estimated from the XRD patterns using the Laue–Bragg equation (Eq. (1)) [42,43].

$$2d\sin(\theta) = n\lambda \tag{1}$$

To evaluate π–π stacking in PTPh-BDTD and PTDE-BDTD, the interlayer spacing (d) between neighboring conjugated layers was calculated from the XRD patterns. The diffraction peaks located at $2\theta \approx 27.21^\circ$ and 26.96° correspond to interlayer spacings of 3.27 and 3.30 Å for PTPh-BDTD and PTDE-BDTD, respectively (Fig. S9c). Notably, PTPh-BDTD exhibits a slightly reduced interlayer spacing compared to the PTDE-BDTD, indicating improved π–π stacking interactions [44,45]. This enhancement is attributed to the phenyl linker in PTPh-BDTD, which promotes more efficient aromatic stacking relative to the ethynylbenzene linkage in PTDE-BDTD.

2.2. Morphology studies

The surface morphology of BDTD-based CMPs was investigated using SEM and TEM. In addition, the presence and distribution of the constituent elements were verified by EDS mapping. (Figs. 3d–k and S10). TEM images show that PTPh-BDTD forms irregular, sheet-like structures (Fig. 3d and e), whereas PTDE-BDTD adopts more uniform rod-like morphologies (Fig. 3f and g). The —C≡C— linkage provides a rigid, linear bridge that constrains the connected aromatic units into a more planar backbone. This higher planarity reduces conformational freedom and promotes uniform packing during assembly, thereby biasing growth in one direction and producing rod-like structures [46,47]. In addition, for PTDE-BDTD, the use of a co-solvent system could influence polymer nucleation and aggregation, thereby promoting a more ordered morphology. Remarkably, both PTPh-BDTD and PTDE-BDTD CMPs

]

exhibit hierarchical porous structures with pore diameters below 10.0 nm, as revealed by low magnification TEM images (Fig. 3d–g). SEM analysis also corroborates these results (Fig. 3h–k). The EDS elemental mapping results validate the effective inclusion of the targeted elemental constituents, as evidenced by a consistent distribution of (S, C, and O) atoms within the CMPs framework (Fig. S10a–h).

2.3. Electrochemical investigations

Electrochemical testing of PTPh-BDTD and PTDE-BDTD was carried out in a three-electrode setup using cyclic voltammetry (CV) and galvanostatic charge–discharge (GCD) methods (Fig. 4). The measurements employed a glassy carbon working electrode, a Pt wire counter electrode, and an Hg/HgO reference electrode in 3.0 M KOH solution. CV profiles were collected between −0.7 and 0.0 V as the scan rate was increased from 5 to 200 mV s^{-1} to probe the redox activity of the BDTD-based CMPs. The observed quasi-reversible redox behavior, arising from Faradaic charge-transfer mechanisms, suggests significant pseudocapacitive behavior in PTPh-BDTD and PTDE-BDTD CMPs (Fig. 4a and b). At a scan rate of 5 mV s^{-1}, PTPh-BDTD shows an anodic peak at −0.38 V and a cathodic peak at −0.43 V. Under the same conditions, PTDE-BDTD exhibits redox peaks at −0.31 V (anodic) and −0.38 V (cathodic) (Fig. 4a and b). Over various scan rates, the generated CMPs retained their distinct shape in the CV curves, indicating outstanding capacitive performance with quick charge–discharge processes [48]. As the scan rate increases, both anodic and cathodic peak positions shift, which can be mainly explained by slower ion transport and charge-transfer kinetics at the electrode–electrolyte interface during rapid polarization [49]. When the scan rate is low, electrolyte ions have sufficient time to penetrate the porous network and reach redox-active sites, so the reaction proceeds closer to equilibrium, and the peaks remain sharp and well-defined. At higher scan rates, ion diffusion cannot keep pace with the potential sweep, producing concentration gradients within the electrode. This polarization increases the required driving force for the redox process and shifts the peak potential to more polarized values [50]. In parallel, ohmic drops in the electrolyte and the electrode's internal resistance become more pronounced at faster scans, further amplifying the peak displacement [51]. Similar scan-rate-dependent shifts have been associated with stronger kinetic limitations, larger apparent charge-transfer resistance, and reduced Faradaic reaction contributions at short time scales [52]. Overall, the observed behavior indicates that charge storage arises from a combination of surface-controlled capacitive processes and diffusion-limited Faradaic reactions, and optimizing this balance is essential for high-performance supercapacitors [53]. GCD measurements were examined to estimate the capacitance performance of the CMP electrodes. The GCD tests were carried out at current densities ranging from 0.5 to 20 A g^{-1} within a potential window of −0.7 to 0 V (Fig. 4c and d). In the alkaline environment, the GCD profiles exhibit pronounced Faradaic behavior, characterized by quasi-symmetric triangular shapes with slight deviations. These deviations mainly arise from the oxidation-reduction behavior during charging and discharging cycling, highlighting the pseudocapacitive characteristics of the electrodes in good agreement with the cyclic voltammetry results [54]. Specific capacitances for the PTPh-BDTD and PTDE-BDTD-based

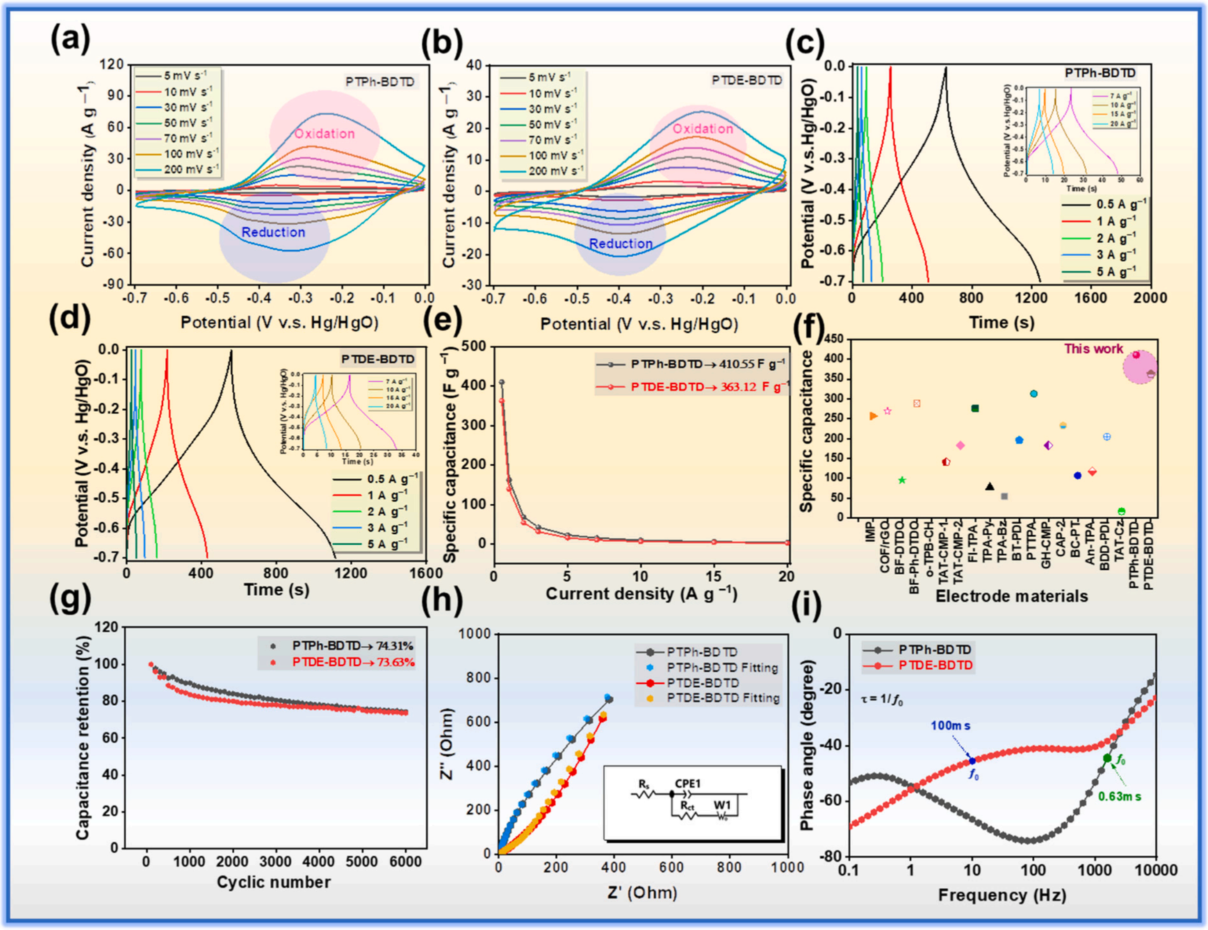

Fig. 4. (a and b) CV characteristics, (c and d) GCD profiles for PTPh-BDTD and PTDE-BDTD CMPs, respectively, (e) specific capacitance values from GCD curve integration, (f) comparison of capacitance with the previously recorded polymers. (g) Cyclic durability measured at 20 A g^{-1}, (h) Nyquist plots along with their fitting curves using the equivalent circuit, and (i) Bode diagrams for PTPh-BDTD and PTDE-BDTD CMPs.

electrodes were obtained from the GCD discharge profiles using Eq. (S1a). [55] At 0.5 A g^{-1}, the calculated capacitances were 410.55 and 363.12 F g^{-1}, respectively (Fig. 4e). These results suggest that the capacitance performance and Faradaic behavior are significantly enhanced by integrating the BDTD redox-active component into the polymer architecture. Moreover, the findings reveal that the linker type, whether Phenyl or ethynylbenzene, significantly affects the electrochemical behavior of the CMP electrodes [45]. The capacitance drops as the current density increases because the shortened charge–discharge time limits ion diffusion and adsorption within the porous electrode [56]. Among the tested materials, PTPh-BDTD delivers the highest capacitance, reaching 410.55 F g^{-1} at 0.5 A g^{-1}, indicating favorable rate behavior [57]. This enhanced response is associated with its phenyl-bridged framework, which provides greater accessible surface area and promotes efficient electronic communication between redox-active units, thereby facilitating charge transfer during cycling. By comparison, PTDE-BDTD shows a lower value of 363.12 F g^{-1}, consistent with its smaller surface area and the different linker geometry. The ethynylbenzene linkage, while preserving conjugation and backbone rigidity, provides less effective interlayer contact than the phenyl bridge, which can reduce electron transport and limit electrolyte access to active sites, thereby decreasing overall charge-storage efficiency. Consequently, diminished interlayer interactions and reduced surface exposure in PTDE-BDTD hinder electron mobility and electrolyte accessibility, thereby lowering charge-transport efficiency. A similar trend was obtained when capacitance values were calculated from the CV curves using Eq. (S1b). As shown in Fig. S11, the PTPh-BDTD and PTDE-BDTD electrodes deliver specific capacitances of 530.18 and 381.56 F g^{-1}, respectively, at 5 mV s^{-1}, further demonstrating the superior charge-storage behavior of PTPh-BDTD. These observations confirm that the electrochemical behavior of BDTD-based CMPs is strongly influenced by the combined effects of surface area and the nature of the π-conjugated linker within their framework. Remarkably, BDTD-based CMPs achieved higher specific capacitances, surpassing those of analogous redox-active materials [57–71], as illustrated in Fig. 4f and Table S8. The small step at the start of the discharge curve is the typical IR drop associated with the cell's equivalent series resistance (ESR) [59]. In a three-electrode configuration, part of the applied current is lost across the uncompensated solution resistance of the electrolyte, resulting in an immediate potential difference between the working and reference electrodes [72]. This effect becomes more evident as the working and reference electrodes are positioned farther apart. Importantly, the initial IR drop mainly reflects resistive losses in the measurement setup and does not directly indicate lower intrinsic conductivity of the active material, reduced charge-storage capability, or degraded interfacial charge-transfer behavior [72]. Considering their notable capacitive properties, we assessed the durability of the PTPh-BDTD and PTDE-BDTD CMP electrode materials over 6000 charge-discharge cycles at 20 A g^{-1}. Fig. 4g shows that PTPh-BDTD and PTDE-BDTD exhibit outstanding cycling stability while maintaining their original specific capacitances at 74.31% and 73.63%, respectively. After prolonged cycling (6000 cycles), the gradual capacitance decay can be attributed to cumulative, irreversible changes at the electrode surface and within the polymer network during repeated Faradaic charging and discharging. In redox-active conjugated polymers and CMP-type frameworks, repeated ion insertion and disinsertion can induce local swelling and contraction, progressively weakening electrical contact among polymer domains and between the active layer and the current collector, thereby increasing internal resistance and reducing charge transport efficiency. In parallel, continuous redox operation may partially alter the chemical environment of the redox-active groups and the conjugated backbone, for example, through over-oxidation, side reactions with electrolyte species, or gradual loss of electrochemically accessible sites, which reduces the effective number of reversible redox centers. In addition, slow pore blocking by trapped ions or reaction by-products can limit electrolyte access to micropores, further decreasing utilization of active sites at long cycling times. Collectively, these effects reduce ion/electron transport kinetics and the fraction of redox sites participating reversibly, resulting in the observed decrease in capacitance after 6000 cycles. Post-mortem FT-IR and SEM analyses were performed after the cycling test to evaluate the chemical and morphological stability of the CMP electrodes. As shown in Fig. S12, the FT-IR spectra of both PTPh-BDTD and PTDE-BDTD after cycling retain the characteristic vibrational bands of the polymer frameworks, including the carbonyl ($C{=}O$) and aromatic backbone features as well as the C—S related signals, with no obvious new absorption bands that would indicate bond cleavage or formation of new functional groups. Only minor changes in band intensity are observed, which can be attributed to differences in electrode loading and possible adsorption of electrolyte residues/water after long-term cycling, rather than a change in the polymer backbone. SEM images (Fig. S13) consistently show that the overall morphologies are largely preserved after cycling: PTPh-BDTD maintains its irregular, aggregated, sheet-like texture, while PTDE-BDTD retains its porous, particulate/clustered architecture. No severe cracking or large-scale structural collapse is evident, suggesting that the capacitance decay is mainly associated with gradual loss of electrochemically accessible sites and increased interfacial/transport resistance during prolonged cycling, rather than catastrophic physical failure of the electrode or extensive chemical decomposition of the CMP framework [73–75].

Additionally, we used electrochemical impedance spectroscopy (EIS) to assess the developed electrodes and evaluate the charge-storage mechanism, as it is a common method for analyzing electrical resistance and ion-diffusion rates within the electrode material. EIS analyses were carried out at a potential with an amplitude of 5 mV (Fig. 4h). The Nyquist plots of the PTPh-BDTD and PTDE-BDTD CMP-based electrodes showed tiny semicircles in the high-frequency region, demonstrating reduced charge-transfer resistance and effective access of electrolyte ions [76,77]. At low frequencies, the Nyquist plots approach a near-vertical line, indicating dominant capacitive behavior and efficient ion storage. The series resistance (*R*s), which mainly reflects the electrolyte resistance in the cell, was obtained from the high-frequency intercept on the Z' axis. The measured *R*s values for PTPh-BDTD and PTDE-BDTD are 4.03 and 4.21 Ω, respectively. Fig. 4h shows the Nyquist plot and the equivalent circuit used for fitting, where *R*s represents the electrolyte resistance, CPE1 is a constant phase element describing the non-ideal double-layer capacitance at the electrode interface, *R*ct denotes the charge-transfer resistance, and Wo is an open Warburg element associated with ion diffusion. From the fitted results, PTPh-BDTD exhibits a slightly lower *R*s (4.11 Ω) than PTDE-BDTD (4.19 Ω). The small difference indicates comparable ohmic losses, as expected, since both measurements were performed with the same electrolyte, concentration, and cell configuration. PTPh-BDTD exhibits a lower charge-transfer resistance (*R*ct) of 6.55 Ω, indicating faster interfacial charge-transfer kinetics and more efficient charge transport. In comparison, PTDE-BDTD shows a higher *R*ct of 8.93 Ω, consistent with greater kinetic resistance and reduced electrochemical efficiency (Table S9). Overall, the lower *R*s and *R*ct values of PTPh-BDTD support its more favorable electrical transport behavior, making it a promising electrode material for energy-storage devices. The conductivity trend was further confirmed by direct electrical conductivity measurements. Room-temperature conductivities were evaluated for the BDTD-based CMP coatings on carbon sheets using a standard four-probe setup. The values obtained for PTPh-BDTD and PTDE-BDTD are 9.0 and 7.5 S cm^{-1}, respectively (Table S10). These conductivities compare favorably with many related organic electrode materials reported in the literature [78–83] (Table S11). Bode plots demonstrate that the relaxation time constants (τ) for the PTPh-BDTD and PTDE-BDTD CMPs were calculated using Eq. (2) [84].

$$\tau = 1/f_0 \tag{2}$$

where f_0 is the frequency at which the phase angle in the Bode plot is

−45°. The calculated relaxation times are 0.63 s and 100 ms, respectively (Fig. 4i), indicating rapid charge propagation and ion diffusion in the BDTD-based CMPs, consistent with the Nyquist analysis.

To gain insight into the charge-storage origin in these CMPs, CV measurements were also carried out for the individual monomers BDTD-2Br, PT-4Br, DEPh-2C≡C, and Ph-2B$(OH)_2$ under the same conditions used for the polymers, namely a three-electrode cell in 3.0 M KOH (Fig. S14). The BDTD-2Br monomer displays a quasi-reversible redox couple, with oxidation and reduction peaks located at −0.35 V and −0.37 V, respectively, at 5 mV s^{-1} (Fig. S14a), confirming its intrinsic redox activity. By comparison, PT-4Br, DEPh-2C≡C, and Ph-2B$(OH)_2$ show nearly rectangular CV curves (Fig. S14b–d), indicative of predominantly non-faradaic behavior within this potential window. These results suggest that the BDTD unit is the primary redox-active component responsible for the Faradaic features observed in the CMP electrodes. Fig. S15 illustrates the charging and discharging behavior of the BDTD active unit. The hydroquinone ($BDTD^{2-}$) is produced by accepting two electrons during reduction. Conversely, the original quinone form BDTD is regenerated by the release of these two electrons during oxidation, demonstrating a fully reversible redox process (Figs. 5a and S15) [59,85]. PT-4Br shows no clear reversible redox features in the CV curves and therefore contributes minimally to the Faradaic charge storage (Fig. S14b). This can be rationalized by the strong electron-withdrawing inductive effect of the four bromine substituents, which lowers the electron density of the conjugated framework and perturbs the electronic structure of the carbonyl centers, thereby destabilizing reduced intermediates [86]. In addition, the highly halogenated planar backbone tends to pack densely in the solid state, which restricts the structural and electronic reorganization required for distinct, reversible redox transitions, leading to weak, broadened, or absent redox responses in electrochemical measurements. Ex situ FTIR measurements collected from the PTPh-BDTD-based electrode at different electrochemical states, including oxidized, reduced, and reoxidized conditions, provide direct support for this mechanism (Figs. 5b, c, and S16). After discharge, the carbonyl stretching band of the quinone unit at about 1646 to 1654 cm^{-1} becomes markedly weaker, consistent with reduction of the BDTD carbonyl groups [87]. When the electrode is reoxidized, this C═O signal largely returns, indicating that the quinone redox conversion is predominantly reversible during cycling. A similar trend is observed for the band near 1271–1280 cm^{-1}, assigned to quinone ring vibrations involving the C—C═O motif, which also decreases upon reduction and is consistent with the formation of the hydroquinone form [88]. In alkaline KOH, quinones can be reduced to dianionic hydroquinone species, and the loss of the neutral quinone structure is reflected by the diminished intensities of both the C═O stretching and the ~1270 cm^{-1} bands.

The provided power-law formula in Eq. (3) illustrates the relationship between current (i) and scan rate (v) utilized to enhance the understanding of the capacitive characteristics of the developed BDTD-based CMPs [89,90].

$$i = av^b \tag{3}$$

Here, *a* and *b* are fitting constants, and *b* is obtained from the slope of the linear plot of log(i) versus log(v). A *b* value close to 1 indicates that charge storage is mainly governed by a surface-controlled capacitive process typical of EDLC behavior. In contrast, a *b* value near 0.5 suggests that the response is dominated by diffusion-limited ion transport within the electrode material. Fig. 6a and d presents the fitted b values for PTPh-BDTD and PTDE-BDTD. For the anodic peaks, the slopes are 0.915 and 0.738, respectively, while for the cathodic peaks, they are 0.837 and 0.660. These intermediate values indicate that charge storage in the BDTD-based CMPs involves a mixed contribution from surface-controlled capacitive effects and diffusion-limited Faradaic processes, consistent with a pseudocapacitive charge-storage mechanism. Further, we established the capacitive contribution ratio under different scan rates using Eq. (4) [91,92]:

$$i(V) = k_1 v + k_2 v^{1/2} \tag{4}$$

where i(V) denotes the CV current-voltage relationship, in which the capacitive contribution is represented as k_1v, and the intercalated charge is represented by $k_2v^{1/2}$. The capacitive contribution was determined to be 54% for PTPh-BDTD and 19% for PTDE-BDTD at a 5 mV s^{-1} scan rate (Fig. 6b and e). PTPh-BDTD exhibits a larger capacitive

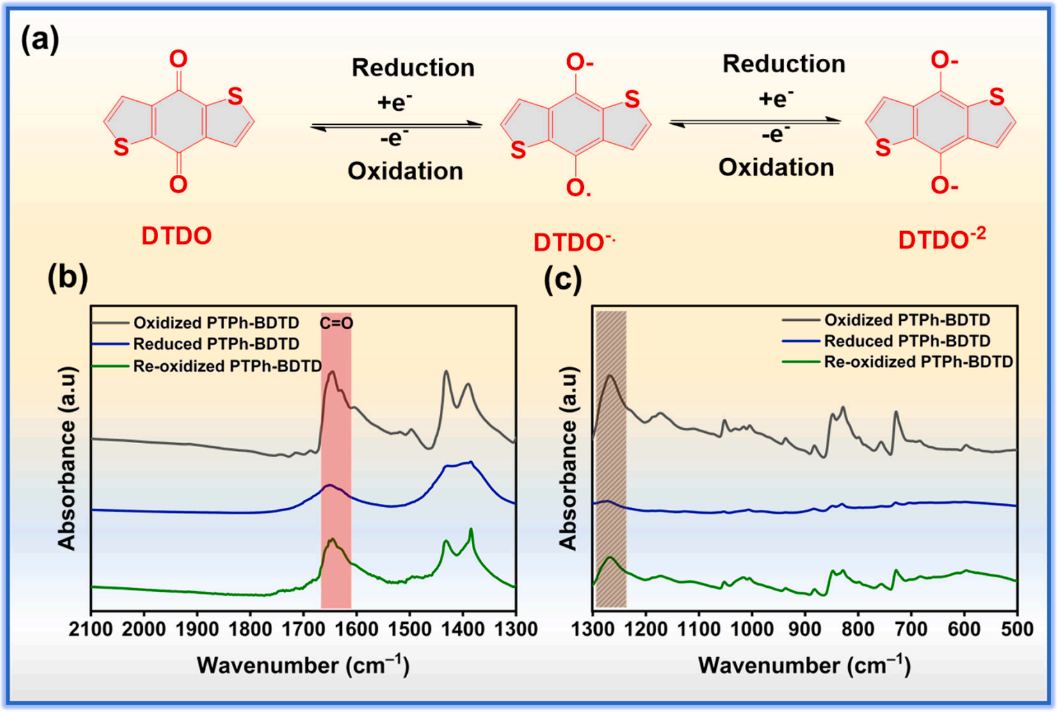

Fig. 5. (a) Proposed redox mechanism of the BDTD. (b–c) Ex-situ FT-IR spectra of PTPh-BDTD-based electrode at oxidized/reduced/re-oxidized states.

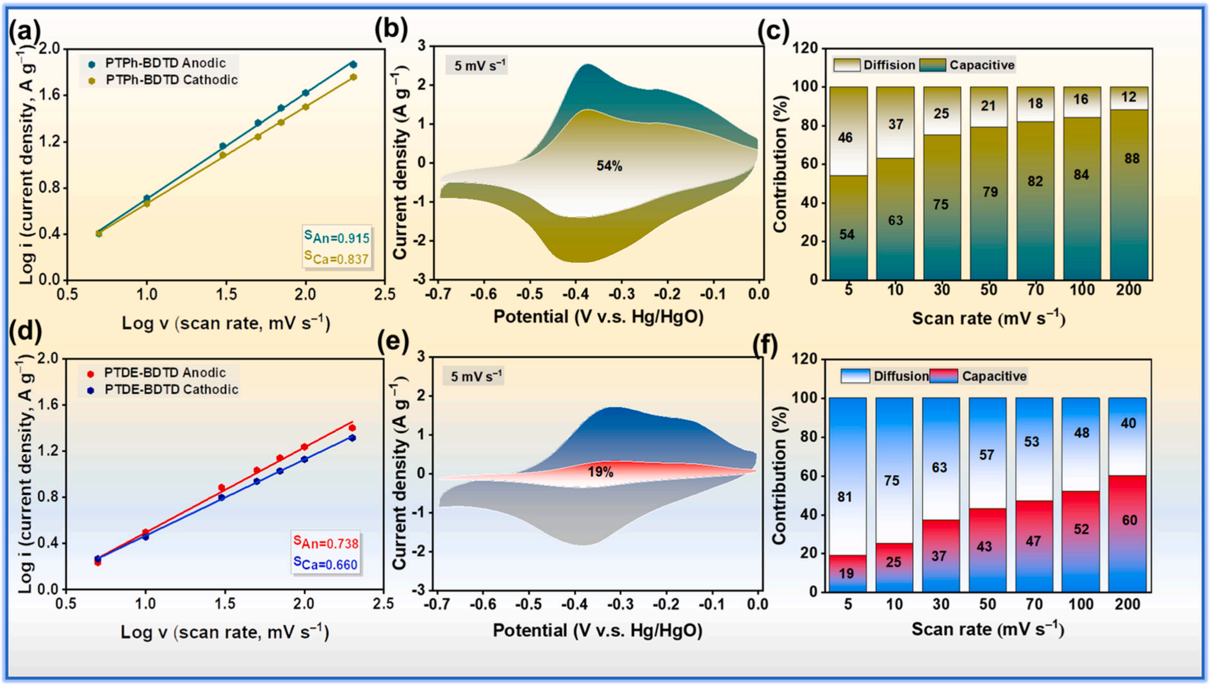

Fig. 6. (a and d) Log(i) against log(v) graphs, (b and e) Capacitive-diffusion contributions examined at 5 mV s^{-1}, (c and f) Charge retention characteristics influenced by capacitive-diffusion mechanisms at different scan speeds for PTPh-BDTD and PTDE-BDTD CMPs, respectively.

contribution, which can be attributed to its higher surface area and more accessible porosity, providing more adsorption and redox-active sites and facilitating rapid electrolyte-ion transport to these sites [56,93]. As the scan rate increases from 5 to 200 mV s^{-1}, the capacitive fraction rises, reaching about 88% for PTPh-BDTD and 60% for PTDE-BDTD (Fig. 6c and f). This shift reflects the reduced time ions have to diffuse into the bulk of the electrode at high scan rates, so charge storage becomes increasingly dominated by surface-controlled processes [59,94]. Conversely, at lower scan rates, ions can penetrate deeper into the electrode framework, increasing the diffusion-controlled contribution and lowering the relative capacitive portion. Overall, the higher surface area together with the phenyl-linker architecture in PTPh-BDTD promotes fast ion transport and greater utilization of surface-accessible redox sites, leading to improved rate performance.

In general, the PTPh-linked CMP exhibits a higher specific capacitance than the ethynylbenzene-linked analogue. Because the BET surface areas are relatively close, the performance enhancement is not governed by surface area alone but instead by differences in framework packing, charge-transport kinetics, and the effective utilization of redox-active sites. In PTPh-BDTD, the phenyl linker promotes a more continuous conjugated pathway and stronger interlayer π–π interactions, which is consistent with its more compact microstructure and the slightly smaller interlayer distance observed by XRD (3.27 Å) compared with PTDE-BDTD (3.30 Å). Elemental analysis and XPS further reveal higher heteroatom contents in PTPh-BDTD (O 17.84% and S 12.64%) than in PTDE-BDTD (O 14.03% and S 8.32%), indicating a higher density of electrochemically addressable carbonyl- and sulfur-related redox sites and thus a larger pseudocapacitive contribution. The impedance results support faster interfacial kinetics for PTPh-BDTD, with a lower charge-transfer resistance (Rct = 6.55 Ω) than PTDE-BDTD (Rct = 8.93 Ω), while both exhibit comparable electrolyte-related series resistance (Rs) under identical conditions. Consistently, four-probe measurements show higher intrinsic electronic conductivity for PTPh-BDTD (9.0 S cm^{-1}) relative to PTDE-BDTD (7.5 S cm^{-1}). Moreover, kinetic analysis shows a markedly higher capacitive contribution for PTPh-BDTD (54% at 5 mV s^{-1}, increasing to ~88% at 200 mV s^{-1}) compared with PTDE-BDTD (19% at 5 mV s^{-1}, increasing to ~60% at 200 mV s^{-1}), demonstrating more efficient utilization of near-surface redox sites at practical rates. By contrast, PTDE-BDTD shows a less compact packing motif, fewer heteroatom-derived redox sites, higher Rct, and lower conductivity, which together limit ion/electron transport and reduce redox-site utilization. Overall, these results demonstrate that high capacitance in CMP-based supercapacitor electrodes is primarily dictated by compact π-stacked microstructures, abundant accessible redox sites, and rapid charge-transfer/electron-transport pathways, rather than by modest differences in BET surface area.

Considering the results mentioned above, PTPh-BDTD CMP demonstrated greater capacitance performance. Consequently, a symmetric supercapacitor (SC) device was assembled in a two-electrode configuration to investigate the potential use of PTPh-BDTD CMP in actual supercapacitor technologies. The mass loadings of both electrodes were carefully optimized. The positive and negative electrodes were fabricated using identical procedures with equal active material mass loadings of approximately 1.0 mg per electrode, ensuring adequate mass balancing ($m^{+} = m^{-}$). Consequently, both electrodes contribute equally to charge storage, and no capacitance mismatch is expected [95,96]. Fig. 7a depicts the device configuration, which consists of two identical PTPh-BDTD CMPs attached to carbon sheets. One acts as the positive electrode, and the other as the negative electrode. A piece of filter paper separates the two electrodes, and 1 M KOH is used as the electrolyte. CV profiles are recorded at scan speeds varying from 5 to 200 mVs^{-1} at a specified voltage difference of +0.8 V. Fig. 7b shows semi-rectangular CV shapes demonstrating reversible pseudocapacitive behavior within the selected potential operating window. The CV responses show minimal distortion at higher scan rates, reflecting fast electrolyte-ion transport and efficient charge uptake. In addition, the charge–discharge curves obtained between 0.3 and 50 A g^{-1} exhibit a nearly triangular shape (Fig. 7c), supporting a pseudocapacitive storage process for the PTPh-BDTD electrode. These pseudocapacitive processes are similar across both electrodes, especially at high current densities, thereby improving overall charge storage. The overall capacitance of the full cell was determined by summing the capacitances of both cathodic and anodic electrodes using Eq. (S4) [55], as illustrated in Fig. 7d and Table S12, yielding values of 112.41, 96.88, 87.18, 65.08, 53.13, 28.99,

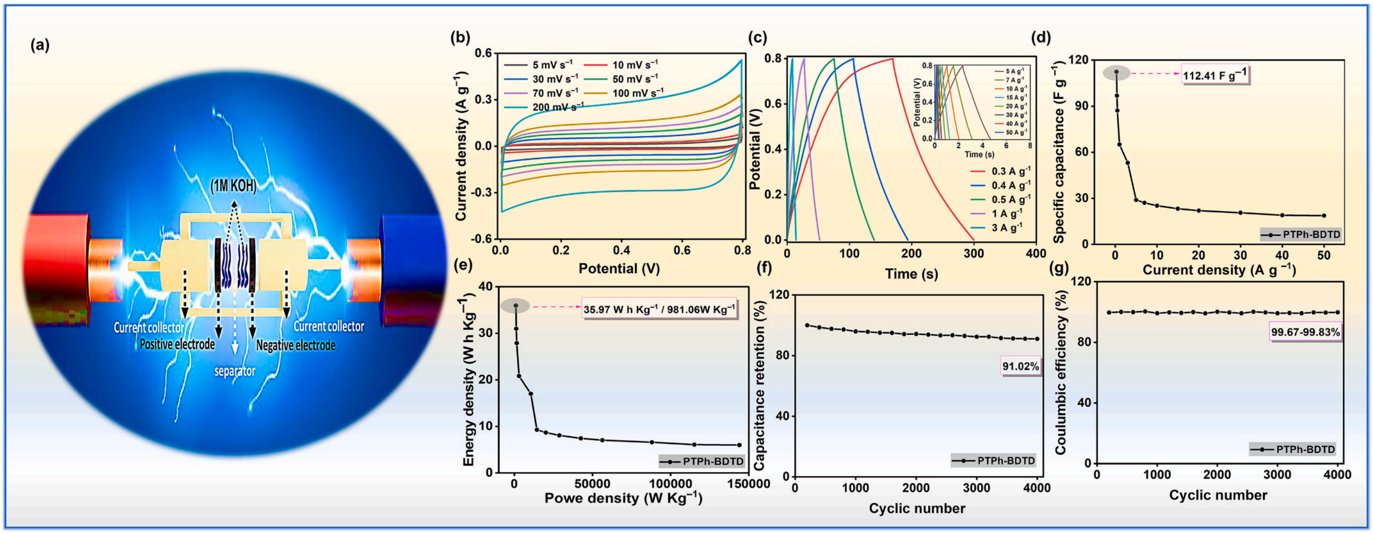

Fig. 7. (a) Diagram illustrating the developed SSC device utilizing PTPh-BDTD CMP, (b) CV curves (c) GCD curves, (d) Specific capacitance, (e) Ragone plots, (f) Stability of charging and discharging up to 4000 cycles at 10 A g^{-1}, and (g) Coulombic efficiency of the PTPh-BDTD-based SC device.

27.12, 25.24, 23.24, 22, 20.62, 19, and 18.74 F g^{-1} at different current densities, confirming the good electrochemical performance of PTPh-BDTD-based device. The CV and GCD responses of the assembled supercapacitor device are less ideal than those measured in the three-electrode configuration, primarily because the full cell has higher internal resistance. This resistance includes contributions from the separator, electrode–electrolyte interfaces, and contact resistances within the device [97]. Moreover, despite careful control during fabrication, the active-material loading differed between the three-electrode and two-electrode measurements because the electrode sizes were different. In the three-electrode test, the working electrode area was small (3.0 mm diameter), so the deposited mass was correspondingly lower. Such minimal loading facilitates efficient ion transport in the electrolyte and reduces internal resistance, thereby producing more ideal CV and GCD profiles [98]. In contrast, the two-electrode setup used electrodes with a larger diameter (1.0 cm = 10 mm), resulting in considerably higher mass loading. The increased thickness and mass of the active material introduce greater ion-diffusion resistance and internal polarization, leading to less-ideal CV and GCD profiles, reduced rate capability, and lower specific capacitance [99]. The PTPh-BDTD–based SC device demonstrates substantially improved capacitance performance relative to earlier reported symmetric porous polymer–based devices (Table S13).

EIS measurements (Fig. S17) show a distinct semicircle at higher frequencies, along with a notably straight line in the lower-frequency range, suggesting minimal charge-transfer resistance and optimal capacitive characteristics. The Ragone plot in Fig. 7e summarizes the device metrics, showing an energy density of 35.97 W h kg^{-1} with a corresponding power density of 981.06 W kg^{-1}. Cycling durability was examined by repeated GCD operation at 10 A g^{-1} for 4000 cycles. As shown in Fig. 7f, the capacitance retention remains ~91.02%, indicating stable long-term operation. Moreover, the PTPh-BDTD-based SC device exhibits outstanding coulombic efficiency (CE) during cycling, with CE values ranging from 99.67 to 99.83% (Fig. 7g). This indicates a highly reversible charge storage behavior. Such near-ideal CE values reflect minimal energy losses due to parasitic processes, including electrolyte decomposition, gas evolution, and irreversible electrode degradation. These results demonstrate effective charge storage with good reversibility and durable electrochemical stability for the PTPh-BDTD-based supercapacitor device.

3. Conclusion

In summary, two PTPh-BDTD and PTDE-BDTD CMPs were successfully designed and synthesized by integrating the electron-deficient benzo[1,2-b:4,5-b′]dithiophene-4,8-dione (BDTD) and the π-extended pyrene-4,5,9,10-tetraone (PT) units through Suzuki and Sonogashira coupling reactions, respectively. The Suzuki coupling reaction was used to synthesize PTPh-BDTD CMP by combining BDTD-2Br, PT-4Br, and Ph-$2(OH)_2$, while the Sonogashira coupling method was employed to develop PTDE-BDTD CMP using BDTD-2Br, PT-4Br, and DEPh-2C$\equiv$C. This work shows that linker engineering and architectural control strongly influence the electrochemical response of these CMPs. The phenyl-linked PTPh-BDTD delivers higher performance, providing a specific capacitance of 410.55 F g^{-1} at 0.5 A g^{-1} with 74.31% retention after 6000 charge–discharge cycles. In addition, the symmetric PTPh-BDTD device achieves 112.41 F g^{-1} with an energy density of 35.97 Wh kg^{-1} and retains 91.02% of its initial capacitance after 4000 cycles, demonstrating good long-term stability. The enhanced performance is attributed to its higher surface area, phenyl-bridge-induced π–π stacking, enhanced heteroatom content, and efficient charge-transport pathways, which collectively improve ion accessibility and redox kinetics. In contrast, PTDE-BDTD with ethynylbenzene linkers exhibited weaker interlayer interactions and lower capacitance, highlighting the sensitivity of electrochemical properties to the linker type. Overall, this study highlights that controlling CMP architecture and selecting suitable π-conjugated linkers are key to regulating charge transport and charge-storage kinetics, offering practical guidance for the rational design of high-performance polymer-based supercapacitor electrodes.

CRediT authorship contribution statement

Yousra M. Nabil: Writing – original draft, Validation, Methodology, Data curation, Conceptualization. **Shimaa Abdelnaser:** Validation, Methodology, Data curation. **Shiao-Wei Kuo:** Software, Resources, Funding acquisition. **Ahmed F.M. EL-Mahdy:** Writing – review & editing, Writing – original draft, Visualization, Supervision, Software, Resources, Methodology, Investigation, Conceptualization.

Declaration of competing interest

The authors declare that they have no known competing financial interests or personal relationships that could have appeared to influence the work reported in this paper.

Acknowledgements

This study gained financial assistance from the National Science and Technology Council, Taiwan, under contract NSTC 112-2221-E-110-005-MY3 and 113-2218-E-110-004-.

Appendix A. Supplementary data

Supplementary data to this article can be found online at https://doi.org/10.1016/j.est.2026.121774.

Data availability

Data will be made available on request.

References

[1] H. Jafarizadeh, E. Yamini, S.M. Zolfaghari, F. Esmaeilion, M.E.H. Assad, M. Soltani, Navigating challenges in large-scale renewable energy storage: barriers, solutions, and innovations, Energy Rpt 12 (2024) 2179–2192, https://doi.org/10.1016/j.egyr.2024.08.019.

[2] S. Gautam, S. Rialach, S. Paul, N. Goyal, MOF/graphene oxide based composites in smart supercapacitors: a comprehensive review on the electrochemical evaluation and material development for advanced energy storage devices, RSC Adv. 14 (2024) 14311–14339, https://doi.org/10.1039/D4RA01027B.

[3] Y. Du, J. Sun, J. Zhao, P. Liu, X. Lv, W. Tian, J. Ji, Flexible graphene-based composite films for energy storage devices: from interfacial modification to interlayer structure design, Chem. Eng. J. 493 (2024) 152704, https://doi.org/10.1016/j.cej.2024.152704.

[4] R. Liu, Z.L. Wang, K. Fukuda, T. Someya, Flexible self-charging power sources, Nat. Rev. Mater. 7 (2022) 870–886. https://www.nature.com/articles/s41578-022-00441-0.

[5] S. Zhong, L. Dai, H. Xu, X.-C. Yang, X. Zheng, S. Wang, Highly porous carbon with selective transformation of nitrogen groups boosts the capacitive performance through boric acid template assisted strategy, J. Energy Storage 97 (2024) 112867, https://doi.org/10.1016/j.est.2024.112867.

[6] C. Li, Q. Yue, Y. Gao, Z. Li, J. Zhang, M. Zhang, S. He, Z. Wu, Y. Yang, J. Gan, C. Li, X. Xue, F. Qi, L. She, C. Zheng, J. Miao, D. Zhang, Z. Xia, H. Pan, Toward rational design of carbon-based electrodes for high-performance supercapacitors, ACS Appl. Mater. Interfaces 17 (2025) 24675–24700, https://doi.org/10.1021/acsami.4c21036.

[7] S.G. Eswaran, M. Rashad, A.S.K. Kumar, A.F.M. EL-Mahdy, A comprehensive review of Mxene-based emerging materials for energy storage applications and future perspectives, Chem. Asian J. 20 (2025) e202401181, https://doi.org/10.1002/asia.202401181.

[8] S. Kabiru Sa'adu, C.S. Khe, M.F. Abd. Shukur, K.F. Chong, C.W. Lai, K.Y. You, N. R. Nik Roseley, E. Aboelazm, Transition metal coordination polymer-derived materials for supercapacitor applications: recent advances and future perspectives, R. Soc. Open Sci. 12 (2025) 250919, https://doi.org/10.1098/rsos.250919.

[9] Z. Fu, H. Zhang, D. Geng, Z. Liu, Z. Zhang, X. Li, C. Yan, Constructing sulfur-heterocyclic aromatic amine polymer with multiple-redox active sites for long-lifespan and all-organic aqueous magnesium ion batteries, Adv. Energy Mater. 15 (2025) 2403934, https://doi.org/10.1002/aenm.202403934.

[10] P. Saini, J.K. Yadav, B. Rani, A. Dixit, Light-driven enhancement in the pseudocapacitance of nanosized ZnO particles and carbon nanotube-based photo-rechargeable supercapacitors, J. Mater. Chem. A 13 (2025) 25543–25558, https://doi.org/10.1039/d5ta03620h.

[11] A. Tundwal, H. Kumar, B.J. Binoj, R. Sharma, G. Kumar, R. Kumari, A. Dhayal, A. Yadav, D. Singh, P. Kumar, Developments in conducting polymer-, metal oxide-, and carbon nanotube-based composite electrode materials for supercapacitors: a review, RSC Adv. 14 (2024) 9406–9439, https://doi.org/10.1039/D3RA08312H.

[12] I.O. Oladele, S.O. Adelani, A.S. Taiwo, I.M. Akinbamiyorin, O.F. Olanrewaju, A. O. Orisawayi, Polymer- based nanocomposites for supercapacitor applications: a review on principles, production and products, RSC Adv. 15 (2025) 7509–7534, https://doi.org/10.1039/D4RA08601E.

[13] M.H. Gharahcheshmeh, K. Chowdhury, Fabrication methods, pseudocapacitance characteristics, and integration of conjugated conducting polymers in electrochemical energy storage devices, Energy Adv. 3 (2024) 2668–2703, https://doi.org/10.1039/D4YA00504J.

[14] I. Hussain, K. Singh, A.C. Mendhe, M.R. Thalji, S. Mandal, I. Ali, A.F.M. EL-Mahdy, P. Rosaiah, M.K. Aslam, T.L. Tamang, K. Zhang, Integration of non-Ti_3C_2 MXene with carbon-based materials for energy storage devices: recent advancements and future aspects, Prog. Solid State Chem. 78 (2025) 100523, https://doi.org/10.1016/j.progsolidstchem.2025.100523.

[15] T.-L. Yang, J.-Y. Chen, S.-W. Kuo, C.-T. Lo, A.F.M. EL-Mahdy, Hydroxyl-functionalized covalent organic frameworks as high-performance supercapacitors, Polymers 14 (2022) 3428, https://doi.org/10.3390/polym14163428.

[16] Y.-M. Wei, D. Kumar, L. Zhang, J.-F. Li, Pseudocapacitive materials for energy storage: properties, mechanisms, and applications in supercapacitors and batteries, Front. Chem. 13 (2025) 1636683, https://doi.org/10.3389/fchem.2025.1636683.

[17] S. Shinde, A.R. Kumar, Advances in cobalt oxide-based supercapacitors: recent strategies and performance enhancement, ChemistrySelect 10 (2025) e01497, https://doi.org/10.1002/slct.202501497.

[18] A. Ali, K. Kumari, M. Ahmad, G.C. Nayak, Functional metal–organic frameworks derived electrode materials for electrochemical energy storage: a review, Chem. Commun. 60 (2024) 13292–13313, https://doi.org/10.1039/D4CC04086D.

[19] S.V. Sadavar, S.Y. Lee, S.J. Park, Advancements in asymmetric supercapacitors: from historical milestones to challenges and future directions, Adv. Sci. 11 (2024) 2403172, https://doi.org/10.1002/advs.202403172.

[20] H. Hao, R. Tan, C. Ye, C.T.J. Low, Carbon-coated current collectors in lithium-ion batteries and supercapacitors: materials, manufacture and applications, Carbon Energy 6 (2024) e604, https://doi.org/10.1002/cey2.604.

[21] S. Jabin, S. Abbas, P. Gupta, S. Jadoun, A. Rajput, P. Rajput, Recent advances in nanoporous organic polymers (NPOPs) for hydrogen storage applications, Nanoscale 17 (2025) 4226, https://doi.org/10.1039/D4NR03623A.

[22] J.H. Wang, C.-L. Chang, Z.W. Zhang, A.F.M. EL-Mahdy, Facile metal-free synthesis of pyrrolo[3,2-b]pyrrolyl-based conjugated microporous polymers for high-performance photocatalytic degradation of organic pollutants, Polym. Chem. 13 (2022) 5300–5308, https://doi.org/10.1039/D2PY00658H.

[23] Y.-Z. Xiao, A.A. Mohammed, S.-W. Kuo, A.F.M. EL-Mahdy, Innovative β-ketoenamine-linked covalent organic frameworks: tailored D1-A-D2-A structure for highly efficient photocatalytic degradation of organic pollutants, Sep. Purif. Technol. 356 (2025) 129950, https://doi.org/10.1016/j.seppur.2024.129950.

[24] J.H. Wang, A.E. Hassan, A.M. Elewa, A.F.M. EL-Mahdy, Donor–acceptor hetero [6] radialene-based three-dimensional covalent organic frameworks for organic pollutant adsorption, photocatalytic degradation, and hydrogen production activity, J. Mater. Chem. A 12 (2024) 14005–14021, https://doi.org/10.1039/D3TA07691A.

[25] B. Reis, R. Frenzel, N. Gerlach, M. Müller, J. Schultz, S. Putwa, J. Weatherby, M. Dasog, S. Schwarz, Gold nanorods decorated by conjugated microporous polymers for infrared responsive cytostatic drug delivery, Langmuir 41 (2025) 2471–2479, https://doi.org/10.1021/acs.langmuir.4c04164.

[26] U. Karatayeva, S.A. Al Siyabi, B.B. Narzary, B.C. Baker, C.F.J. Faul, Conjugated microporous polymers for catalytic CO_2 conversion, Adv. Sci. 11 (2024) 2308228, https://doi.org/10.1002/advs.202308228.

[27] X. Luo, Y. Zhang, S. Zhou, P. Wang, D. Wang, P. Gu, A near-infrared-II light-response BODIPY-based conjugated microporous polymer for enhanced photocatalytic degradation of cationic dyes and H_2O_2 production, Chem. Commun. 60 (2024) 7910–7913, https://doi.org/10.1039/D4CC02912G.

[28] W. Zhang, H. Zuo, Z. Cheng, Y. Shi, Z. Guo, N. Meng, A. Thomas, Y. Liao, Macroscale conjugated microporous polymers: controlling versatile functionalities over several dimensions, Adv. Mater. 34 (2022) 2104952, https://doi.org/10.1002/adma.202104952.

[29] M. Li, J. Ma, J. Wang, X. Wei, W. Lu, Conjugated microporous polymer-based fluorescent probe for selective detection of nitro-explosives and metal nitrates, ACS Appl. Mater. Interfaces 17 (2025) 4033–4043, https://doi.org/10.1021/acsami.4c19789.

[30] M.G. Kotp, N.L. Torad, J. Lüder, A.A.M. El-Amir, W. Chaikittisilp, Y. Yamauchi, A. F.M. EL-Mahdy, A phenazine-conjugated microporous polymer-based quartz crystal microbalance for sensitive detection of formaldehyde vapors at room temperature: an experiment and density functional theory study, J. Mater. Chem. A 11 (2023) 764–774, https://doi.org/10.1039/D2TA07966F.

[31] T.A. Gaber, L.R. Ahmed, A.F.M. EL-Mahdy, Efficient faradaic supercapacitor energy storage using redox-active pyrene-and benzodithiophene-4, 8-dione-tethered conjugated microporous polymers, J. Mater. Chem. A 11 (2023) 19408–19417, https://doi.org/10.1039/D3TA03198E.

[32] X. Zhang, L. Teng, J. Chen, X. Gong, H. Liu, J. Duan, L. Jiang, X. Hou, W. Lyu, Y. Liao, Conjugated microporous polymers via a one-pot Buchwald-Hartwig/Suzuki-Miyaura double-coupling for high-performance flexible supercapacitors, J. Colloid Interface Sci. 701 (2025) 138671, https://doi.org/10.1016/j.jcis.2025.138671.

[33] Y. Zhang, W. Luo, Z. Hu, H. Sun, Z. Zhu, J. Li, R. Jiao, A. Li, Template synthesized spider network-like conjugated microporous polymers composite membranes with high mechanical properties for separation and flexible wearable devices, Chem. Eng. J. 520 (2025) 166151, https://doi.org/10.1016/j.cej.2025.166151.

[34] X. Mi, J. Li, W. Lyu, L. Xu, Y. Liu, C. Qian, J. Yu, W. He, J. Feng, Y. Liao, Boosting Fenton-like reaction via enhanced charge transfer in donor-acceptor polyaniline-like conjugated microporous polymers, Appl. Catal. B-Environ. Energy 378 (2025) 125530, https://doi.org/10.1016/j.apcatb.2025.125530.

[35] R.K. Karthick, U. Rajaji, T.-Y. Liu, V. Kumar, Charge injection dynamics in oxygen-functionalized and heteroatom-doped reduced graphene oxide and their impact on supercapacitor performance: an experimental and DFT investigation, J. Electroanal. Chem. 977 (2025) 118848, https://doi.org/10.1016/j.jelechem.2024.118848.

[36] S. Uppugalla, R. Pothu, R. Boddula, M.A. Desai, N. Al-Qahtani, Nitrogen and sulfur co-doped activated carbon nanosheets for high-performance coin cell supercapacitor device with outstanding cycle stability, Emerg. Mater. 6 (2023) 1167–1176, https://doi.org/10.1007/s42247-023-00503-1.

[37] H. Qin, X. Zuo, Y. Song, W. Li, M. Liao, X. Mo, Y. Zhao, H. Chen, Regioselectively dibrominated bis-acenaphthoquinone diimides: a strong acceptor unit for n-type conjugated polymers, Dyes Pigments 222 (2024) 111889, https://doi.org/10.1016/j.dyepig.2023.111889.

[38] H. Peng, V. M. -García, J. Raya, H. Wang, H. Guo, F. Richard, P. Samorì, A. Ciesielski, Supramolecular engineering of cathode materials for aqueous zinc-ion hybrid supercapacitors: novel thiophene-bridged donor–acceptor sp^2 carbon-

linked polymers, J. Mater. Chem. A 11 (2023) 2718–2725, https://doi.org/10.1039/D2TA09651J.

[39] Z. Yu, M. Li, Y. Han, H. Peng, Y. Geng, X. Wu, Z. Yan, Z. Zhu, Redox-active donor-acceptor conjugated microporous polymer for high-voltage and high-rate symmetric all-organic lithium-ion battery, Mater. Today Energy 53 (2025) 101995, https://doi.org/10.1016/j.mtener.2025.101995.

[40] F. Kang, Y. Zhang, Z. Chen, Z. Bai, Q. Gu, J. Yang, Q. Liu, Y. Ren, C.-S. Lee, Q. Zhang, Umpolung of a covalent organic framework for high-performance cathodic sodium ion storage, Chem. Sci. 16 (2025) 7711–7719, https://doi.org/10.1039/D5SC01195G.

[41] X. Cao, X. Zhang, C. Duan, H. Xu, W. Yuan, Y. Tao, W. Huang, Simple phenyl bridge between cyano and pyridine units to weaken the electron-withdrawing property for blue-shifted emission in efficient blue TADF OLEDs, Org. Electron. 57 (2018) 247–254, https://doi.org/10.1016/j.orgel.2018.03.027.

[42] Y. Oaki, K. Sato, Amorphous conjugated polymer networks as an emerging class of polymer nanostructures, RSC Appl. Polym. 3 (2025) 78–91, https://doi.org/10.1039/D4LP00276H.

[43] D. Zhou, K. Zhang, S. Zou, X. Li, H. Ma, Conjugated microporous polymers: their synthesis and potential applications in flexible electrodes, J. Mater. Chem. A 12 (2024) 17021–17053, https://doi.org/10.1039/D4TA02085E.

[44] L. Jing, P. Li, Z. Li, D. Ma, J. Hu, Influence of π–π interactions on organic photocatalytic materials and their performance, Chem. Soc. Rev. 54 (2025) 2054–2090, https://doi.org/10.1039/D4CS00029C.

[45] Y.M. Nabil, S. Abdelnaser, A.A. Mohammed, S.-W. Kuo, A.F.M. EL-Mahdy, Engineering redox-active benzo [1, 2-b: 4, 5-b′] dithiophene-based conjugated polymers: tuning porosity and linker architecture for high-performance supercapacitors, J. Mater. Chem. A 13 (2025) 26337–26349, https://doi.org/10.1039/D5TA03907J.

[46] F. Mohajer, M.M. Heravi, V. Zadsirjan, N. Poormohammad, Copper-free Sonogashira cross-coupling reactions: an overview, RSC Adv. 11 (2021) 6885–6925, https://doi.org/10.1039/D0RA10575A.

[47] A.F.M. EL-Mahdy, C. Young, J. Kim, J. You, Y. Yamauchi, S.-W. Kuo, Hollow microspherical and microtubular [3+3] carbazole-based covalent organic frameworks and their gas and energy storage applications, ACS Appl. Mater. Interfaces 11 (2019) 9343–9354, https://doi.org/10.1021/acsami.8b21867.

[48] D. Patra, S.K. Pati, S. Muduli, S. Mishra, S. Park, Highly planar pseudocapacitive semiconducting polymer electrodes toward symmetric supercapacitors with a wide range of operating potentials, Chem. Eng. J. 482 (2024) 149162, https://doi.org/10.1016/j.cej.2024.149162.

[49] K.J. Aoki, J. Chen, Y. Liu, B. Jia, Peak potential shift of fast cyclic voltammograms owing to capacitance of redox reactions, J. Electroanal. Chem. 856 (2020) 113609, https://doi.org/10.1016/j.jelechem.2019.113609.

[50] T.T.T. Vuong, V.V. Thang, T.N. Tran, N.M. Hieu, P.L. Nguyen, T.V.B. Phung, High-performance supercapacitors from composites derived from recycled alkaline batteries, Sci. Rep. 15 (2025) 41600, https://doi.org/10.1038/s41598-025-25571-7.

[51] D.A. Bograchev, Y.M. Volfkovich, S. Martemianov, Diagnostics of supercapacitors using cyclic voltammetry: modeling and experimental applications, J. Electroanal. Chem. 935 (2023) 117322, https://doi.org/10.1016/j.jelechem.2023.117322.

[52] Q. Tayyaba, N. Sultan, S. Siddique, A.R. Khan, Insights into the electrochemical performance of manganese dioxide coated metallic foils as potential electrodes for supercapacitors, J. Appl. Electrochem. 55 (2025) 905–917, https://doi.org/10.1007/s10800-024-02211-y.

[53] C. Cougnon, Impact of the scan rate on the stability window of an electrical double-layer capacitor, Energies 16 (2023) 5687, https://doi.org/10.3390/en16155687.

[54] R. Nasser, H. Zhou, A.B.G. Trabelsi, F.H. AlKallas, H. Elhouichet, J.-M. Song, Engineering preparation of the nanocomposite containing $CoWO_4$ nanodots and its high electrochemical activities, J. Energy Storage 68 (2023) 107763, https://doi.org/10.1016/j.est.2023.107763.

[55] S. Roldán, D. Barreda, M. Granda, R. Menéndez, R. Santamaría, C. Blanco, An approach to classification and capacitance expressions in electrochemical capacitors technology, Phys. Chem. Chem. Phys. 17 (2015) 1084–1092, https://doi.org/10.1039/C4CP05124F.

[56] B. Pattanayak, P.-A. Le, D. Panda, F.M. Simanjuntak, K.-H. Wei, T. Winie, T.-Y. Tseng, Ion accumulation-induced capacitance elevation in a microporous graphene-based supercapacitor, RSC Adv. 12 (2022) 27082–27093, https://doi.org/10.1039/D2RA04194D.

[57] C. Li, J. Yang, P. Pachfule, S. Li, M.-Y. Ye, J. Schmidt, A. Thomas, Ultralight covalent organic framework/graphene aerogels with hierarchical porosity, Nat. Commun. 11 (2020) 4712, https://doi.org/10.1038/s41467-020-18427-3.

[58] J. Jin, R. Wang, K. Yu, Y. Tao, P. Zhang, L. Ke, J. Yang, M. Shi, Imine-based conjugated plymer enables efficient removal of ammonium ion via capacitive deionization, Sep. Purif. Technol. 353 (2025) 128290, https://doi.org/10.1016/j.seppur.2024.128290.

[59] S.-X. Liao, A.F.M. EL-Mahdy, Redox-active conjugated microporous polymers featuring a precise pore size for high-performance supercapacitor energy storage, ACS Appl. Energy Mater. 8 (2025) 3074–3086, https://doi.org/10.1021/acsaem.4c03232.

[60] H.-L. Ho, C.-C. Wang, C.-C. Hu, G.-S. Liou, Substitution and isomeric effects of triarylamine polyamides for electrochromic supercapacitors and heat-shielding applications, J. Mater. Chem. A 13 (2025) 27377–27385, https://doi.org/10.1039/D5TA04660B.

[61] X.-C. Li, Y. Zhang, C.-Y. Wang, Y. Wan, W.-Y. Lai, H. Pang, W. Huang, Redox-active triazatruxene-based conjugated microporous polymers for high-performance supercapacitors, Chem. Sci. 8 (2017) 2959–2965, https://doi.org/10.1039/C6SC05532J.

[62] A.F. Saber, A.F.M. EL-Mahdy, S.-W. Kuo, Development of heteroatom-rich fluorene-based benzoxazine-linked porous organic polymers as potential candidates for energy storage, J. Taiwan Inst. Chem. Eng. 168 (2025) 105935, https://doi.org/10.1016/j.jtice.2024.105935.

[63] M.G. Kotp, S.U. Sharma, J.-T. Lee, A.F.M. EL-Mahdy, S.-W. Kuo, Triphenylamine-based conjugated microporous polymers as dye adsorbents and supercapacitors, J. Taiwan Inst. Chem. Eng. 134 (2022) 104310, https://doi.org/10.1016/j.jtice.2022.104310.

[64] S.K. Pati, D. Patra, S. Muduli, S. Mishra, S. Park, Conjugated polymer electrodes fabricated using rylene-based acceptors toward high energy and power density symmetric supercapacitors operable in an organic electrolyte environment, J. Mater. Chem. A 12 (2024) 21165–21175, https://doi.org/10.1039/d4ta03711a.

[65] X. Cheng, C. Du, J. Li, Y. Zhang, W. Xu, J. Zhang, H. Shi, G. Zhang, L. Zhang, Dual redox-centered p (thiophene-TPA) conjugated polymers for high-performance flexible electrochromic supercapacitors, Chem. Eng. J. 510 (2025) 161744, https://doi.org/10.1016/j.cej.2025.161744.

[66] M. Zhang, T. Zhao, J. Dou, Z. Xu, W. Zhang, X. Chen, X. Wang, B. Zhou, Bottom-up construction of conjugated microporous polyporphyrin-coated graphene hydrogel composites with hierarchical pores for high-performance capacitors, ChemElectroChem 6 (2019) 5946–5950, https://doi.org/10.1002/celc.201901586.

[67] W. Liu, M. Ulaganathan, I. Abdelwahab, X. Luo, Z. Chen, S.J.R. Tan, X. Wang, Y. Liu, D. Geng, Y. Bao, J. Chen, K.P. Loh, Two-dimensional polymer synthesized via solid-state polymerization for high-performance supercapacitors, ACS Nano 12 (2018) 852–860, https://doi.org/10.1021/acsnano.7b08354.

[68] A.F. Saber, Y.-F. Chen, L. Mabuti, S.V. Chaganti, S.U. Sharma, J. Lüder, J.-T. Lee, S.-W. Kuo, A.F.M. EL-Mahdy, Engineering carbonyl-rich conjugated microporous polymers with a pyrene-4, 5, 9, 10-tetraone building block as highly efficient and stable electrodes for energy storage, Mater. Adv. 6 (2025) 607–616, https://doi.org/10.1039/d4ma00928b.

[69] A.F. Saber, S. Abdelnaser, A.F.M. EL-Mahdy, S.-W. Kuo, One-pot synthesis of heteroatom-rich anthraquinone-based benzoxazine-linked porous organic polymers for high-performance supercapacitors, Electrochim. Acta 511 (2025) 145397, https://doi.org/10.1016/j.electacta.2024.145397.

[70] D. Patra, S.K. Pati, S. Muduli, S. Mishra, G.-H. Kim, H. Bae, T. Kim, S. Park, Enhanced anodic charge storage in asymmetric hybrid supercapacitor featuring dione–diimide-based electron deficient conjugated polymers, J. Mater. Chem. A 13 (2025) 24694–24705, https://doi.org/10.1039/d5ta01316j.

[71] A.F. Saber, S.-W. Kuo, A.F.M. EL-Mahdy, Microporous carbons derived from nitrogen-rich triazatruxene-based porous organic polymers for efficient cathodic supercapacitors, J. Mater. Chem. A 12 (2024) 15373–15385, https://doi.org/10.1039/D4TA01242.

[72] M.R. Islam, S. Afroj, N. Karim, Scalable production of 2D material heterostructure textiles for high-performance wearable supercapacitors, ACS Nano 17 (2023) 18481–18493, https://doi.org/10.1021/acsnano.3c06181.

[73] Z. Song, L. Miao, H. Duan, Y. Lv, L. Gan, M. Liu, Multielectron redox-bipolar tetranitroporphyrin macrocycle cathode for high-performance zinc-organic batteries, Angew. Chem. 136 (2024) e202401049, https://doi.org/10.1002/ange.202401049.

[74] P. Liu, Z. Song, Q. Huang, L. Miao, Y. Lv, L. Gan, M. Liu, Multi-H-bonded self-assembled superstructures for ultrahigh-capacity and ultralong-life all-organic ammonium-ion batteries, Energy Environ. Sci. 18 (2025) 5397–5406, https://doi.org/10.1039/D5EE00823A.

[75] W. Du, Q. Huang, Y. Lv, Z. Song, L. Gan, M. Liu, High-voltage multi-S-heterocyclic covalent organic frameworks for zinc–organic batteries with high energy density and ultralong life, Energy Environ. Sci. (2026), https://doi.org/10.1039/D5EE04802H.

[76] J. Guo, N. Ming, S. Yuan, P. Zhou, K. Huo, J. Xu, Vertical-array channel engineering of wood-structured thick electrode to assemble high-performance supercapacitors, Chem. Eng. J. 514 (2025) 163200, https://doi.org/10.1016/j.cej.2025.163200.

[77] M. Shahid, A. Zaib, J. Mughal, A. Tariq, U. Waqas, S.M. Ramay, S. Atiq, Optimizing $BiFeO_3$ nanostructures with reduced graphene oxide for sustainable energy storage applications, J. Energy Storage 132 (2025) 117888, https://doi.org/10.1016/j.est.2025.117888.

[78] Y. Gao, Q. Hui, Q. Liu, X. Xia, R. Li, Y. Chen, D. Wang, H. Liu, Insights into the heteroatom-incorporated storage mechanism of hierarchically interconnected porous conjugated polymer networks for extremely stable potassium-ion storage, Chem. Eng. J. 483 (2024) 149200, https://doi.org/10.1016/j.cej.2024.149200.

[79] S. Abdelnaser, S.-W. Kuo, A.F.M. EL-Mahdy, Conjugated microporous polymers incorporating pyridine moieties for efficient faradaic supercapacitor energy storage, J. Power Sources 635 (2025) 236535, https://doi.org/10.1016/j.jpowsour.2025.236535.

[80] V.K. Venkatareddy, H. Parsimehr, A. Ignaszak, R.M. Rao, Near-IR absorbing tetraene-linked π-conjugated porous polymers for energy storage and electrical conductivity, Chem. Commun. 61 (2025) 125–128, https://doi.org/10.1039/d4cc05074f.

[81] H. Cai, H. Tang, T. Wang, C. Xu, J. Xie, M. Fu, X. Luo, Z. Hu, Y. Zhang, Y. Deng, G. Li, C. Liu, F. Huang, Y. Cao, An n-ype open-Shell conjugated polymer with high-spin ground-state and high intrinsic electrical conductivity, Angew. Chem. 136 (2024) e202402375, https://doi.org/10.1002/anie.202402375.

[82] A.A. Kocaeren, D.Ş. Bahçeci, B. Kızılkaya, F. Doğan, Electrochemical polymer synthesis using thiophene and pyrrole/carbazole: their electrochemical behaviours and capacitor performance, J. Electroanal. Chem. 967 (2024) 118486, https://doi.org/10.1016/j.jelechem.2024.118486.

[83] Y. Zhong, C. Li, F. Yang, L. Guan, S. Jin, Covalent pyrimidine frameworks via a tandem polycondensation method for photocatalytic hydrogen production and proton conduction, Small 19 (2023) 2204515, https://doi.org/10.1002/smll.202204515.

[84] Z. Husain, A.R.S. Raheman, K.B. Ansari, A.B. Pandit, M.S. Khan, M.A. Qyyum, S. S. Lam, Nano-sized mesoporous biochar derived from biomass pyrolysis as electrochemical energy storage supercapacitor, Mater. Sci. Energy Technol. 5 (2022) 99–109, https://doi.org/10.1016/j.mset.2021.12.003.

[85] J. Zhan, A.F.M. EL-Mahdy, Redox-active benzodithiophene-4,8-dione-based conjugated microporous polymers for high-performance faradaic supercapacitor energy storage, Chem. Eng. J. 473 (2023) 145124, https://doi.org/10.1016/j.cej.2023.145124.

[86] T. Nakayama, B. Uno, Electronic inductive and resonance effects of substituents on concerted two-proton-coupled electron transfer between electrogenerated superoxide and hydroquinone derivatives in N,N-dimethylformamide, Chem. Eng. J. 491 (2024) 152201, https://doi.org/10.1016/j.cej.2024.152201.

[87] J. Bitenc, N. Lindahl, A. Vizintin, M.E. Abdelhamid, R. Dominko, P. Johansson, Concept and electrochemical mechanism of an Al metal anode–organic cathode battery, Energy Storage Mater. 24 (2020) 379–383, https://doi.org/10.1016/j.ensm.2019.07.033.

[88] A. Vizintin, J. Bitenc, A.K. Lautar, K. Pirnat, J. Grdadolnik, J. Stare, A. R. -Vitanova, R. Dominko, Probing electrochemical reactions in organic cathode materials via in operando infrared spectroscopy, Nat. Commun. 9 (2018) 661, https://doi.org/10.1038/s41467-018-03114-1.

[89] G. Nabi, A. Siddiqa, M. Tanveer, A. Nadeem, K.S. Ahmad, Manganese substitution effects on structural and electrochemical performance of $CoFe_2O_4$ for promising supercapacitor electrode materials, Inorg. Chem. Commun. 168 (2024) 112850, https://doi.org/10.1016/j.inoche.2024.112850.

[90] G. Nabi, H. Ahmed, W. Ali, A. Nadeem, R.S. Ahmad, K.S. Ahmad, Ta-ions doping impacton structural modifications and bandgap tuning of $NiCo_2O_4$ hexagonal nanosheets for high rated pseudocapacitor electrodes, J. Energy Storage 100 (2024) 113696, https://doi.org/10.1016/j.est.2024.113696.

[91] Y. Cai, G. Zhao, Q. Yuan, J. Zhao, Elaborate designed sandwich structural faradic material NPC/NiMn-LDH/MXene for enriched ion accessible transfer pathways in capacitive deionization, Chem. Eng. J. 484 (2024) 149491, https://doi.org/10.1016/j.cej.2024.149491.

[92] S. Wang, L. Zhao, Y. Lei, Z. Li, G. Wang, N-doped MnO_2 with abundant oxygen vacancies achieves high-capacity and stable ammonium ion capture by capacitive deionization, Sep. Purif. Technol. 329 (2024) 125204, https://doi.org/10.1016/j.seppur.2023.125204.

[93] M.P. Adhikari, S. Shahi, R. Ma, J.P. Hill, K. Ariga, L.K. Shrestha, Ultrahigh surface area self-nitrogen-doped nanoporous carbon materials from *Macrotyloma uniflorum* (Horse gram) seed for high-performance supercapacitor applications, J. Power Sources 631 (2025) 236239, https://doi.org/10.1016/j.jpowsour.2025.236239.

[94] Ö. Başgöz, A. Güngör, Ö. Güler, E. Erdem, High-entropy alloys and oxides as supercapacitor electrodes: a structural and electrochemical perspective for energy storage, Adv. Sustain. Syst. 9 (2025) 2500201, https://doi.org/10.1002/adsu.202500201.

[95] X. Yang, T. Lv, J. Qiu, High mass-loading biomass-based porous carbon electrodes for supercapacitors: review and perspectives, Small 19 (2023) 2300336, https://doi.org/10.1002/smll.202300336.

[96] K.K.P. Kumar, N.K. Arkoti, N. Chundi, G. Elsa, M. Vijayakumar, M. Karthik, S. Sakthivel, Dual functional superhydrophobic and superorganophilic porous graphene carbon nanocomposite electrodes for unprecedented high-voltage supercapacitor with superior rate capability, Chem. Eng. J. 513 (2025) 162859, https://doi.org/10.1016/j.cej.2025.162859.

[97] S. Sharma, P. Chand, Supercapacitor and electrochemical techniques: a brief review, Results Chem. 5 (2023) 100885, https://doi.org/10.1016/j.rechem.2023.100885.

[98] P. Xu, S. Luo, J. Liang, D. Pan, B. Zou, J. Li, High-performance 2.2 V asymmetric supercapacitors achieved by appropriate charge matching between ultrahigh mass-loading Mn_3O_4 and sodium-jarosite derived FeOOH, Adv. Funct. Mater. 34 (2024) 2313927, https://doi.org/10.1002/adfm.202313927.

[99] W. Li, M. Wu, W. Yang, M. Zhao, X. Lu, Effects of electrode mass loading on the self-discharge of supercapacitors, Electrochim. Acta 438 (2023) 141550, https://doi.org/10.1016/j.electacta.2022.141550.